

Optical cartography of the Northern Galactic Plane: IPHAS stellar density maps as tests of Galactic models

H. J. Farnhill¹ et al.

¹Centre for Astrophysics Research, Science and Technology Research Institute, University of Hertfordshire, College Lane, Hatfield, AL10 9AB, U.K.

Draft last compiled 9 May 2015

ABSTRACT

Galactic models are becoming increasingly powerful tools to interpret the large amounts of data produced by the new generation of Galactic Plane surveys. In order to test the performance of the Besançon model of Galactic population synthesis, along with a number of extinction models, incompleteness-corrected density maps derived from IPHAS broad-band photometry were produced, and are presented here.

Key words: Galaxy: stellar content – extinction.

1 INTRODUCTION

The positioning of the Solar System almost in the equatorial plane of the Milky Way places a significant obstacle in the way of understanding the structure of our own galaxy. Despite the fact that the disc of the Milky Way is effectively the largest object in the night sky, offering vastly superior angular resolution compared to that achievable for any other galaxy, sightlines at low Galactic latitude remain a challenge to decipher because of large and variable amounts of dust extinction. Given that the formation and maintenance of galactic discs is an important problem in galaxy evolution (review reference), an improved vision of our own galactic disc is needed. And as our wider home, it is of interest in its own right.

The reliable empirical determination of the 3-dimensional distribution of the Milky Way’s interstellar dust, needed to make sense of the disc, is now becoming possible through the increasingly sophisticated analyses of comprehensive digital survey data (Drimmel & Spergel 2002 - check, Marshall et al 2006, Sale et al 2009, 2014). In the next 5–10 years, these advances will complement the astrometric harvest being gathered by the Gaia mission and usher in a much better, sharper vision of the 3D Galactic disc. Nevertheless, the anticipated Gaia parallax precision at fainter magnitudes ($100\mu\text{arcsec}$ at $G \sim 19$) will still leave stars beyond the first 1–2 kpc with distances known to a precision worse than 10–20 percent. Accordingly, it remains useful to supplement our knowledge through the application of other methods that can test predictive Galactic models. One of these, that puts to good use the uniquely detailed view we have of the Galactic disc, is the exploitation of magnitude-limited star counts. This approach has been applied successfully in the past and it has been influential in both guiding

and testing the content of Galactic models (Robin et al 2003, Czekaj et al 2014).

So far, deeper optical star-count mapping has only been carried out in the southern Galactic plane (DENIS reference?). The options to conduct a well-calibrated stellar density mapping of the northern sky are now appearing with the advent of digital imaging surveys (SDSS, Pan-STARRS - refs). The greater challenge is at low Galactic latitudes, but this is now tractable as the 1 arcsec angular-resolution IPHAS (Drew et al 2005), and UVEX (Groot et al 2009) surveys approach completion. In particular, the recent release of IPHAS DR2 (Barentsen et al 2014), offering a uniform photometric calibration of the northern Galactic Plane in r , i (and $H\alpha$), provides the basis for a precise and deep stellar density map across almost 1800 square degrees.

In this work, we describe the construction of r , i stellar density maps at a range of resolutions, up to a maximum resolution of 1 square arcminute, based on IPHAS DR2. In order that this mapping is not hampered by variable observing conditions and similarly variable source losses, great care has been taken to make corrections for incompleteness and confusion by evaluating the results of artificial source injection tailored to every survey field. Because this technical process has so far only been discussed superficially in the literature (see e.g. *ref* for the fullest description to date), we present a reasonably full description of how we arrive at the position- and magnitude-dependent corrections applied. This is presented in section 3 (after a brief restatement of the main features of the IPHAS survey in section 2).

The way in which the corrected r , i stellar density maps are assembled is described in section 4. This includes the specifications of the maps and pointers on how to access them. In i band our map reaches down to 18th mag (Vega system), a limit that roughly corresponds to Gaia $G \sim 19$ (see Appendix B). In section 5, the maps are subjected to first comparisons with Galactic model predictions. This is

* E-mail: h.farnhill@herts.ac.uk

attempted using distinct prescriptions of the 3-d distribution of interstellar extinction in order to gain an impression of how influential the choice of 3D extinction map can be. Interestingly, the results from this limited exploration are already mixed. It is found that outside the Solar Circle ($\ell > 90^\circ$ in the north), the agreement between star counts and model prediction is quite good – but at the lowest Galactic longitudes examined, significant discrepancies appear. The paper ends in section 6 with a brief discussion of these first results and a summary.

2 OBSERVATIONS

2.1 IPHAS broad-band photometry

The most recent release, DR2, of the INT/WFC Photometric H α Survey of the Northern Galactic Plane (IPHAS) was presented by Barentsen et al (2014), while the basic specification of IPHAS was set down by Drew et al (2005). This survey, conducted using the Wide Field Camera (WFC) mounted on the Isaac Newton Telescope (INT) in La Palma, provides photometry of the complete Northern Galactic Plane within the latitude range $-5^\circ < b < +5^\circ$, in narrow-band H α and broadband Sloan r and i . It is the broadbands that are the focus of this paper. The typical 5σ magnitude limit reached in the survey is 21.2 in r and 20.0 in i , achieved at a median seeing of 1.1 arcsec. The typical external photometric precision of DR2 is close to 0.03 magnitudes, as judged by comparisons with SDSS DR9 data. In Galactic longitude terms this survey spans the range $30^\circ < \ell < 215^\circ$. In time it will be fully complemented by the VPHAS+ survey (Drew et al 2014) covering the Southern Galactic Plane and Bulge.

Whilst IPHAS is certainly uniform in its execution, the weather at the telescope represented an important variable. The observations were obtained via standard allocations of time, with the result that a wide variety of observing conditions are contained within the survey database. Thanks to the opportunity to obtain repeats of fields exposed in poor conditions, it was possible to apply quality cuts in the preparation of IPHAS DR2 so as to omit clearly inferior data, whilst still achieving over 92% coverage of the survey footprint. Even so, there is still a broad quality range within DR2 in terms of both measured widths of the point spread function (PSF), and limiting magnitude (for full details, see Barentsen et al. (2014)). This variation, along with over a factor of ten decline in the typical observed stellar density along the Northern Plane from $\ell \sim 30^\circ$ out to the Anticentre (see figure 3 in González-Solares et al. (2008)), makes it important to restore uniformity to the measured star counts through careful position-dependent completeness corrections. Achieving this, along with the development and application of an algorithm that ensures reliable source counting without duplication and proper accounting for small gaps and other irregularities in the data, is the main labour presented here (described also by Farnhill 2015, PhD Thesis).

The first step in this process is to establish a working definition of a detected 'star' in the survey data.

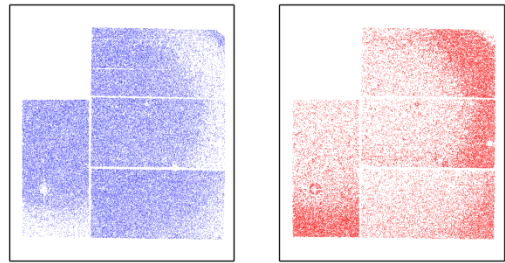


Figure 1. Distributions of sources classified as stellar ($rClass = -1$, blue) and non-stellar ($rClass = +1$, red) in the r' -band for IPHAS field 49750_aug2004a

2.2 On morphological classification and the expected number density of extra-galactic sources

A fraction of sources detected in DR2 fields are known to be misclassified as non-stellar towards field edges – this is due to progressive distortion in the PSF with increasing distance from the optical axis (OA) of the INT/WFC system. This pattern of behaviour has a small impact on the final DR2 catalogues, which provide primary detections that are selected according to a criterion of lowest distance to the optical axis. But when counting stellar (morphological class -1) sources from a single field to produce a stellar density map the issue of progressive misclassification has to be tackled. Fig. 1 shows an example of a field exhibiting this problem.

Assuming a constant ratio of stellar to non-stellar sources applies in reality across any one field, comparisons between 5 sq. deg. regions at field centres and edges revealed occasional misclassification of several hundred sources. Of course, some of these objects are not misclassified – they can be genuine examples of galaxies presenting as extended objects. To determine the expected number of galaxies detected in a similar area, galaxy counts were taken from Yuda et al. (2001), down to the 5σ r' - and i' -band limits of IPHAS, and then extinguished by the median Schlegel et al. (1998) extinction values for all fields (corrected using the Schlafly & Finkbeiner (2011) recalibration). Based on median limiting magnitudes, ~ 1 extragalactic source is predicted per 5 sq. deg. region. Against stellar densities typically orders of magnitude larger, this is very small. It was therefore regarded as safe to include 'non-stellar' +1 classified sources for density mapping purposes – the losses that would be suffered on leaving them out, in fields similar to that depicted in Fig. 1, are much larger than is the likely contribution from galaxies.

3 COMPLETENESS CORRECTION

Genuine astronomical sources falling within IPHAS detection limits can fail to appear in the resulting photometric catalogues for a number of reasons. Detector issues can prevent sources from being picked up: the WFC is a 4-CCD mosaic leaving gaps between the component detectors, and there are also bad columns and regions of vignetting that will hinder detection. In the majority of such cases (but

not quite all), missing sources will be picked up in the offset partner pointing, or in the overlap with a neighbouring field.

More significant and pervasive losses affecting the final star counts are those due either to confusion promoted by high stellar densities or to statistical sensitivity losses at the faint limit for detection. In the Galactic plane at lower longitudes, where the stellar density in IPHAS can reach up to 500,000 per square degree, confusion will be especially important and liable to determine the effective magnitude limit. Outside the Solar Circle where the typical stellar density is 50,000 per square degree, confusion is no more than marginally significant: the median 1.1 arcsec PSF implies 70 'beams' per source, to be compared with the rule of thumb confusion threshold of 30 per source (see Hogg 2001). Both kinds of incompleteness are exacerbated by relatively poor seeing. We first consider confusion and its estimation in some detail, before going on to describe our chosen method of incompleteness correction based on artificial source injection.

3.1 Confusion, as estimated from the nearest-neighbour distribution

Confusion, the effect of background noise caused by unresolved sources, scales with source density (Condon 1974). For randomly distributed sources, the probability of finding a given number of neighbours within a certain distance can be described by a Poisson distribution, which leads to the nearest neighbour distribution

$$n(\theta) = 2\rho^2 \Omega \pi \theta e^{-\rho \pi \theta^2} \quad (1)$$

as presented in Bahcall (1986).

Fig. 2 shows this distribution for an area with the effective area of the WFC field of view (0.29 sq. deg.) containing varying numbers of sources. It can be seen that increasing the density of sources increases the number of nearest neighbours at small separations, while suppressing the number at greater separations, thereby pulling in the peak separation value, θ_{max} . Equation 1 holds for a population of sources randomly distributed regardless of brightness. In practice, where the distribution of source brightnesses is described by a power law, the susceptibility of a source to confusion increases with decreasing brightness: a limiting faint magnitude must be chosen in order to define a meaningful confusion rate.

In order to reproduce the theoretical distribution (Eqn. 1), all sources in the area Ω would need to be recovered. This will never be the case in dense fields, which will modify the observed distribution in the sense that the smallest separations will be under-reported - appearing to relatively boost the proportion of nearest neighbours at larger values of θ .

Three test cases are shown in Fig. 3: these IPHAS fields, located around $\ell \sim 32^\circ$, were chosen because they lie in a region of the survey containing fields spanning a wide range of densities. The $n(\theta)$ distributions were generated by selecting subregions of the CCDs such that a border of width $30''$ was excluded, and the nearest neighbour was identified for each of the sources in the central subregion. This approach avoids the case where sources close to CCD edges have their nearest neighbour assigned to a source in the CCD area, when in fact its nearest neighbour on the sky is located beyond the detector edge. When identifying the nearest neighbours

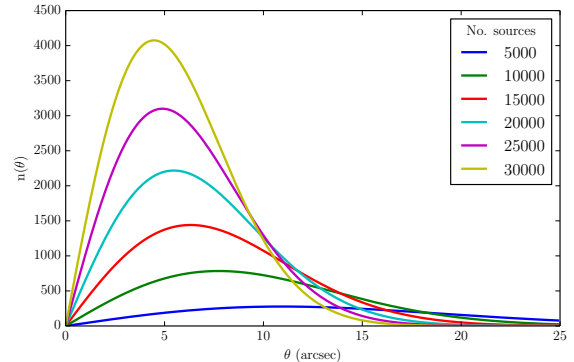


Figure 2. Theoretical distribution (see Equation 1) of nearest neighbour distances for an area with the effective area of a WFC image, for fields containing varying numbers of sources.

for each source in the central region, the border region was searched as well.

The fields are displayed in order of increasing density. The left-most field, 4198.jul2004, contains 3,966 sources - a number sufficiently low that confusion would not be expected to make a significant contribution to incompleteness. Fields 4450o.jul2009 and 4285.jun2004, containing 24,291 and 49,150 sources respectively, suffer from increasing levels of confusion. The overplotted theoretical distribution gives an idea of the amount of confusion; at low field densities, the empirical and theoretical distributions agree quite well, while at higher densities the theoretical distributions clearly predict closer nearest neighbours than measured.

While the observed nearest neighbour distribution is affected significantly by confusion most significantly at smaller ($\lesssim 10''$) separations, the observed number of nearest neighbours at larger separations will be less affected. Hence, the theoretical distribution best fitting the tail at large θ values comes close to describing the field as if confusion were not an issue. We have exploited this property as a means to gauge confusion loss at small separations. We have fitted distributions generated from Eqn. 1 to the observed distributions at $> 10''$ separation, varying ρ such that the number of sources in a field ranged from half to twice its observed value. By calculating χ^2 for each fit at large separations, the best fitting value of ρ was found for each, identifying the correction that should be applied for confusion.

Fig. 4 shows the effect of confusion on the survey as a whole. Best fitting $n(\theta)$ distribution (corresponding to a theoretical unconfused source count) was obtained for each IPHAS field, allowing a picture to be built up of the impact of confusion. The statistic chosen to represent the magnitude of the correction is the ratio of $\frac{\text{observed}}{\text{predicted}}$ sources, where the "predicted" source count is the count corresponding to the best fit theoretical $n(\theta)$ distribution. In order to understand the variation in confusion at different limiting magnitudes m_0 , fits were performed on sources brighter than respectively 18th, 19th and 20th magnitudes in r' , in addition to fits across all sources.

In a perfect survey capable of deblending overlapping sources, all fields would exhibit zero confusion, with their curves jumping from zero to 100% of all fields at a ratio of 1.0. In reality some sources will always be lost to confu-

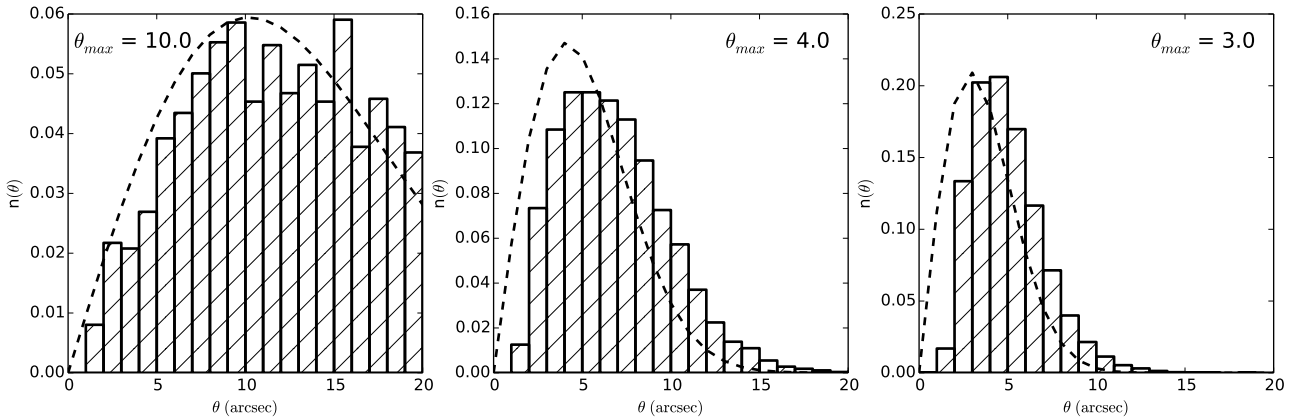


Figure 3. Nearest neighbour distributions for three IPHAS fields, normalised to allow the overplotting of theoretical distribution (dashed line). Density of fields increase from left to right.

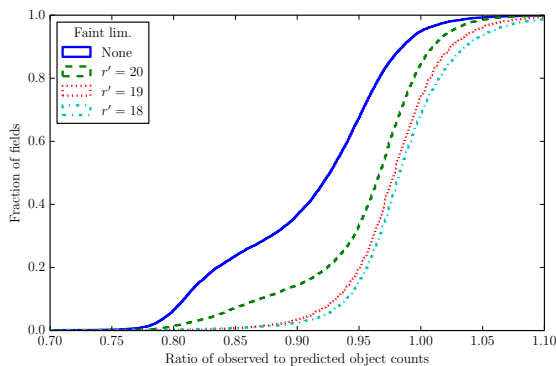


Figure 4. Cumulative histogram of $\frac{\text{observed}}{\text{predicted}}$ source counts, where the predicted counts were estimated by fitting Equation 1 to the tail of the nearest neighbour distribution. The four curves represent the ratio as determined for sources down to three different limiting magnitudes, and an instance where no limit was placed on the magnitude of sources.

sion, with the impact increasing the higher the density of objects. Fainter objects suffer more from confusion losses as their PSFs are more likely to be lost in the vicinity of brighter sources, in addition to their intrinsically higher densities (see Fig. 6 for examples of the magnitude distributions of IPHAS fields). Fig. 4 demonstrates this behaviour as the incompleteness takes hold for a greater number of fields as the cut-off magnitude m_0 is increased.

For a fraction of fields at all values of m_0 , the best fit to their nearest neighbour distributions indicates a lower predicted number of sources than is actually observed. WHY DO WE THINK THIS IS: THE UNCERTAINTY REFERRED TO NEXT (AT 18, 19th MAG?) The maximum ratio returned is ~ 1.1 , for fields which can be seen to lie in regions of lowest density when plotted spatially. These fields would be expected to return a corresponding best fit ratio of 1.0, suggesting that the fitting to the $n(\theta)$ distribution tails has an associated uncertainty of $\sim 10\%$; such an un-

certainty renders this approach for correcting source counts unreliable. Indeed Fig. 4 can be regarded as a demonstration that, as a general rule, at $r < 18$ the impact of confusion in IPHAS is small while (as might be expected) it is close to ubiquitous at $r > 20$. Source counts in the i band are higher thanks to the lower extinction – the same plot for this band shows that confusion becomes a minor consideration at $i < ?????$ (A NUMBER, PLEASE, HYWEL)

3.2 Other approximate measures of completeness

There exists a formalism for correcting for the number of sources lost to confusion, based upon Eqn. 1, given by

$$\rho = -\rho' \frac{\log(1 - 4\rho' \pi \theta_{FWHM}^2)}{4\pi \theta_{FWHM}^2} \quad (2)$$

where ρ is the actual source density, ρ' is the observed density, and θ_{FWHM}^2 is the seeing in which the field was observed. The expression was derived in Irwin & Trimble (1984), and used to correct the observed $n(\theta)$ distributions directly in González-Solares et al. (2008). Clearly fields with poorer seeing and higher densities will be subject to larger corrections; (González-Solares et al. 2008) reported that the IPHAS Initial Data Release fields suffering from greatest confusion were missing 41% of their sources.

However Eqn. 2 does not hold for the entire $[\rho', \theta_{FWHM}]$ space covered by all IPHAS DR2 fields – it breaks down in dense fields, where the seeing is worse than the median. Fig. 5 shows the variation of the correction term for the range of parameters relevant to DR2. The white region shows the parameter space in which Eqn. 2 is not applicable, where

$$4\pi\rho\theta^2 > 1 \quad (3)$$

Although this condition will not be met so often, the fact that it will mean that applying eqn. ?? across the survey is not viable.

An approach used in several previous surveys (Ruphy et al. 1997; Cambrésy et al. 2002; Lucas et al. 2008) is to estimate the completeness limit by taking the magnitude

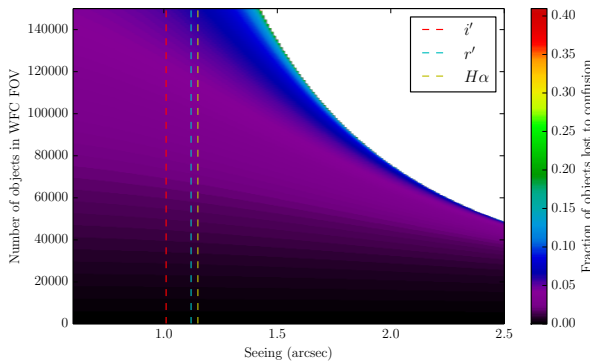


Figure 5. Correction term in Eqn. 2 for the range of $n_{src} = \rho' \times \Omega_{WFC}$ and θ_{FWHM} . Median seeings for each filter are marked by vertical lines. White region denotes domain where Equation 3 is true and Equation 2 breaks down.

distribution of sources and identifying at which magnitude the distribution begins to drop off.

As part of a study of stellar populations in the Galactic Plane, Ruphy et al. (1997) commented on the need for simulated images for a quantitative study of completeness in their frames, although they opted instead to report a completeness limit derived from the star count histograms of uncrowded fields. This approach may serve well in studies of limited sky regions, or if sources fainter than this putative completeness limit can be excluded without causing problems. Ruphy et al. (1997) mentioned that confusion due to crowding was the only source of incompleteness for which they account, choosing to ignore the “slight variations due to the observing conditions” (an approach unfeasible for IPHAS).

Cambrésy et al. (2002) estimated their completeness from the turnover of 2MASS magnitude distributions, and reason that their density maps would show imprints of individual observations had they overestimated their limiting magnitudes. This would certainly be the case for IPHAS - without any limiting magnitudes in place, the field-to-field variation of densities is extremely obvious. In applying a similar treatment of incompleteness, Lucas et al. (2008) quote the 90% completeness limit of the UKIDSS Galactic Plane Survey, noting that in uncrowded fields the modal depths vary by 0.25 mag due to observing conditions. This method still depends heavily on the turnover in the magnitude distribution, assuming that sensitivity is the only cause of turnover, and relies on “visually extrapolating” the histogram.

A single completeness statistic as provided by Lucas et al. (2008) could be used to apply a uniform completeness correction, although this assumes that all fields in a survey suffer from the same degree of incompleteness. Even if this were indeed the case, only the count of sources brighter than the given completeness limit could be corrected; it is not possible with this information to correct the count going deeper.

Fig. 6 shows the magnitude distributions for three IPHAS fields. A visual inspection would suggest that incompleteness sets in at \sim 20th mag or fainter in r and at \sim 19th in i and $H\alpha$. Attempts to automate the determina-

tion of turnover magnitude for all fields are hampered by the facts that the mode of these distributions are dependent on the chosen binning, and that the magnitude distributions of many fields plateau before dropping off. But it is already clear from the previous section and Fig. ?? that the full picture is more complicated, with confusion not ruled out at magnitudes of 18 to 19 and that there is good reason to address correction rigorously on a field by field basis.

3.3 Artificial source injection

A thorough treatment of incompleteness in any survey requires measuring its sensitivity to sources over the entire magnitude range of interest - this is best achieved by simulating observations and then processing these simulated frames in the same way as the original data. This method was used (in addition to the magnitude distribution method discussed in §3.2) and described by Harvey et al. (2006) as part of a study of interstellar clouds observed by Spitzer.

Such an approach is much more powerful, as statistics can be returned on magnitude bins, rather than on the entire magnitude distribution down to a specified faint limit. This requires the simulation of sources of all magnitudes, resembling the real data as closely as possible, without being too costly to generate in either computing power or time.

For the purposes of correcting the density map, the completeness of each field was assessed using the images and catalogues of CCD 4 only. Using only one of the WFC CCDs per field cuts the processing time by a factor of four, bringing the total time necessary to compute the completeness of the entire survey down to a little over one week. Due to the fact that DR2 preferentially selects sources from the centre of fields (closer to the optical axis), CCD 4 was selected as the chip to represent each field (see §?? for further discussion).

This approach to completeness calculation was divided into steps. First the typical properties of an image were determined, and used to generate synthetic sources that closely resemble genuine stellar sources (Section 3.4). The parameters of these synthetic sources were recorded and then catalogues generated from the new frames containing synthetic objects. The tables of synthetic source parameters were cross-matched against the newly generated catalogues, and the rate of recovery measured (Section 3.5). The fraction recovered at different magnitudes will allow a completeness curve to be built up for each field, and uniformly computed corrections to be applied across the entire survey.

3.4 Simulating stellar sources

The complexity of simulating stellar sources depends on the accuracy with which the real sources are to be recreated. A first order approximation might be a circular PSF characterized by a two-dimensional Gaussian, requiring only three parameters - FWHM, peak height and centroid coordinates. A cursory glance at the reduced IPHAS frames reveals that a perfectly circular PSF will not reproduce realistic stellar sources - a more complex approximation is needed (see Fig. 7).

The parameters returned by the aperture photometry performed on the DR2 images suggest what might need to be included to accurately recreate a stellar source:

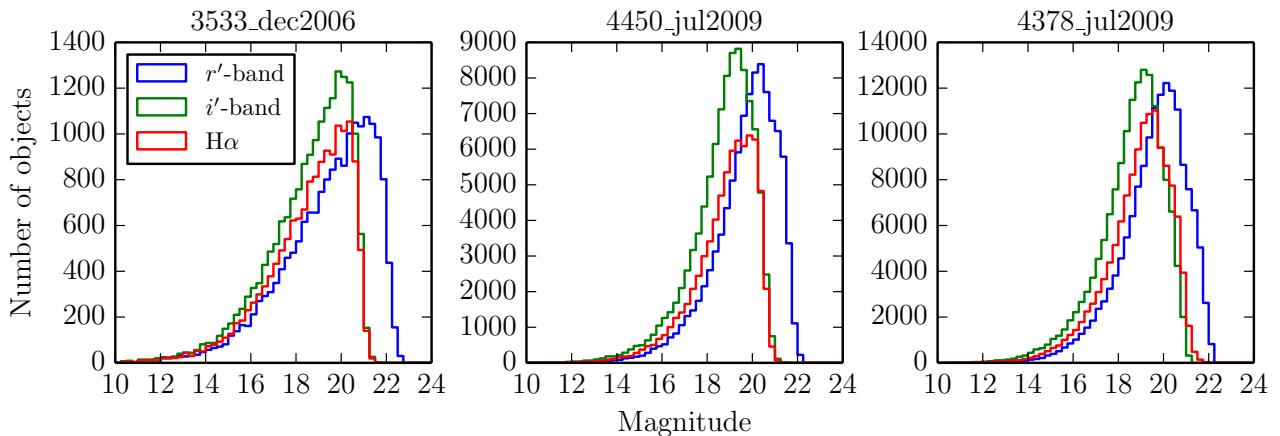


Figure 6. Magnitude distributions for three IPHAS fields of increasing density. From left to right, fields have r' -band source counts of 18,113, 99,061 and 153,430. A requirement that sources counted here have $n_{\text{Bands}} > 1$ places the greatest constraint on i' -band counts, as redder sources are picked up in the i' -band only.

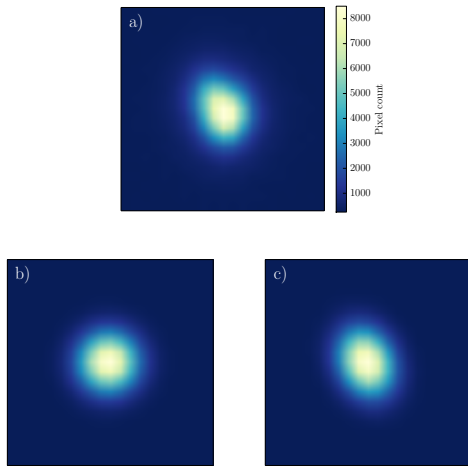


Figure 7. **a)** 16th magnitude source from an IPHAS field. **b)** Simulated source generated using best-fit parameters of a 2D circular Gaussian. **c)** source generated using best-fit parameters of a 2D elliptical Gaussian.

- Flux
- FWHM
- Ellipticity
- Position angle
- Sky background level
- Coordinates (or pixel position on detector).

The choice of each is described below.

Ideally measuring the completeness using artificial sources would be done by adding a single source at a time, verifying whether or not it is detected. This process would be repeated as many times as required to obtain decent statistics, for the entire magnitude range of interest. This would be the route taken in the absence of any limitations on either time or computing resources.

The limiting factor in the completeness investigation is the time taken by the IMCORE routine, which takes ~ 20 seconds to read in an IPHAS image, run its background estimation routines and generate a catalogue. Adding a single source at a time would require ~ 20 s, multiplied by both the number of magnitude bins that are being considered, and the number of sources needed in each bin for sufficient statistics. This would push the time required to generate the number of sources detailed in Table 1 to ~ 65 hours for a single field.

To reduce the cost, multiple sources needed to be inserted into each image simultaneously. It was necessary to ensure that not too many sources were inserted at any one time; inserting too high a number would modify the intrinsic properties of the image - for example, probing the completeness of an originally sparse image with a high number of artificial sources inserted would not return statistics useful for understanding the original image. The value of $\frac{\delta n}{n_{\text{image}}}$ needed to be kept sufficiently low, where δn is the number of artificial sources added to the image, and n_{image} is the number of sources present in the original image. The quality control information available for DR2 fields report that the most sparsely populated fields contain more than 1000 stars. This is not an extremely constraining limit; a maximum of up to 50 stars was chosen as a value that would keep $\frac{\delta n}{n_{\text{image}}}$ below 0.05 for all fields.

Allowing up to 50 sources per artificial source injection increases efficiency by reducing the number of IMCORE runs needed. The low value of $\frac{\delta n}{n_{\text{image}}}$ renders unworkable an approach of inserting sources based on the pre-existing magnitude distribution of the sources in the image - the number of runs required to inject artificial sources in this fashion would be significantly higher than the approach actually adopted; the requirement that $\frac{\delta n}{n_{\text{image}}} < 0.05$ would mean a very small number of bright (~ 12 mag) sources being injected in each run, requiring a large number of runs to obtain usable statistics at brighter magnitudes. The approach adopted was to split the magnitude range of interest into magnitude bins 0.25 mag wide, inserting sources from only one bin at a time.

Magnitude bin				
Start	End	N	M	No. sources
12.0	12.25	10	10	100
12.25	12.5	10	10	100
:	:	10	10	100
14.5	14.75	10	10	100
14.75	15.0	10	10	100
15.0	15.25	20	10	200
:	:	20	10	200
16.25	16.5	20	10	200
16.5	16.75	30	10	300
:	:	30	10	300
17.75	18.0	30	10	300
18.0	18.25	40	10	400
:	:	40	10	400
18.75	19.0	40	10	400
19.0	19.25	50	10	500
19.25	19.5	50	10	500
19.5	19.75	50	15	750
19.75	20.0	50	15	750
20.0	20.25	50	20	1000
:	:	50	20	1000
20.75	21.0	50	20	1000
Total:		410		12300

Table 1. Number of artificial sources added per magnitude bin. *No. sources* denotes total number that will be generated over *M* runs. *N* is the number of sources that will be added to each image, which will be repeated *M* times. A total of 123000 are added per field, across 410 images containing artificial sources.

Table 1 details the number of sources inserted per image, and the number of artificial images that were generated for each magnitude bin. The total numbers per magnitude bin were increased as sources become progressively fainter. This was achieved by increasing the number of artificial sources injected per run until the limit of 50 sources was reached. At this point the number of runs was increased to raise the total number of sources injected in the faintest bins, minimizing the noise at the faint end of the completeness curve, where the most significant corrections will be necessary.

The setup detailed in Table 1 requires around 2.2 hours (~ 20 s \times 410 IMCORE runs). For the 14,115 fields that make up DR2, this results in a total computing time of ~ 31000 hours. Using the computer cluster available within the Science & Technology Research Institute at the University of Hertfordshire, a large number of CPUs are available to run such jobs. Utilizing 128 CPUs simultaneously brings the total time to estimate completeness for the entire survey in a single band to ~ 10 days.

3.4.1 Flux

The relation between total flux and magnitude was determined per field by fitting a power law to the photometry returned by IMCORE.

Mention that flux height is initially used? It doesn't have

to be, and if code is rewritten for publication this step could be removed.

As discussed in Section 3.4, pre-defined numbers of sources are inserted in each magnitude bin. In order to insert a source of a given magnitude *m*, it is necessary to understand what flux that source would have to recover a measurement of *m*. The magnitude of an object is determined by

$$m = ZP - 2.5 \times \log_{10} \frac{c}{t} - APCOR - PERCORR \quad (4)$$

where *ZP* is the photometric zeropoint of the image, *c* is the measured counts within the defined aperture, *t* is exposure time in seconds, *APCOR* and *PERCORR* are small correction terms.

The *ZP* of a given field is calculated based on an average of photometric standards observed on the night of observation. *APCOR* is an aperture correction term calculated by IMCORE, which uses the curve-of-growth of stellar sources to determine the correction required to transform the chosen aperture measurement to total flux. *PERCORR* is a sky calibration correction, obtained by comparing dark sky regions with the median across each CCD. *ZP*, *APCOR* and *PERCORR* are all provided in the catalogue headers. *Too much information?*

3.4.2 Full-width at half-maximum

Initially the parameters of genuine sources in IPHAS frames were determined by fitting elliptical two-dimensional Gaussian profiles to each source detected by IMCORE, building up lists of best fit parameters for the purpose of generating realistic artificial sources.

Parameters of sources were excluded from the lists if they exhibited one of the following behaviours:

- Source position returned further than 5 pixels from the position reported by IMCORE
- these fits are likely to have been disturbed by nearby sources
- Object where the peak value of the best-fit Gaussian is > 55000 counts
- this is the regime for the WFC where bright sources saturate, distorting the PSF.
- If the position angle is measured to be exactly zero
- in these cases the fit is assumed to have failed.

The best fit FWHM values returned for the semi-major and semi-minor axes of the sources were gathered, and Gaussians fit to their distributions. Fig. 8 shows the distributions for four IPHAS fields, in addition to the central positions of the best fit Gaussians.

This would work across all fields, but the fitting of 2D Gaussians to each source in the frame took too long. Since the FWHM values obtained in this way were in good agreement with the median FWHM as determined by IMCORE, it was decided that taking this value as representative of the entire field was sufficient. Fig. 8 shows how the median FWHM values fall within 1σ of the best fit Gaussian distributions for four randomly selected IPHAS DR2 fields.

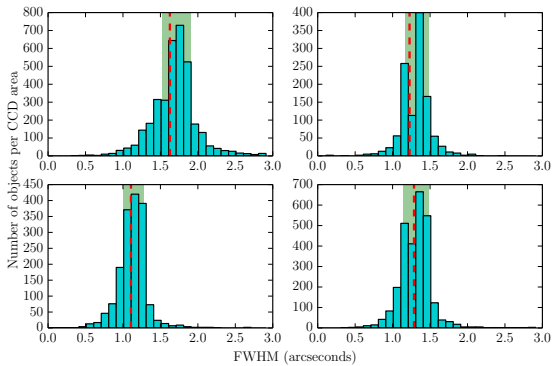


Figure 8. Distribution of best fitting FWHM values in arcseconds for sources from four randomly selected IPHAS DR2 fields. Values were obtained by fitting elliptical Gaussians to every stellar source in CCD4 of the IPHAS field. FWHM values reported here are for the Gaussian profile along the semi-major axes of the sources. **Red lines** denote the median FWHM as determined by IMCORE for CCD4. **Green shaded areas** highlight the regions centred on the best fit FWHM for the distributions, and encompass the area $\pm\sigma$.

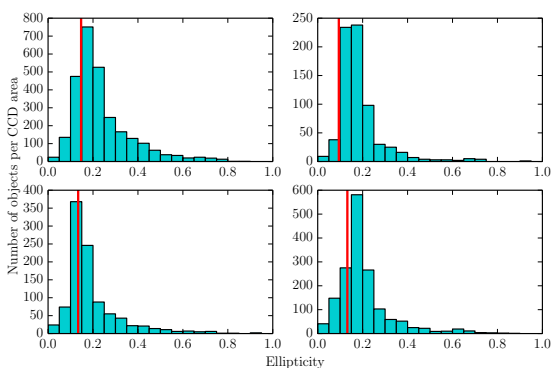


Figure 9. Distribution of ellipticities for all stellar sources in four randomly selected IPHAS fields. Ellipticities were computed from the profiles of the elliptical Gaussians best fitting each object along their semi-major and -minor axes. **Red lines** denote the median ellipticities for CCD4 of each field as determined by IMCORE.

3.4.3 Ellipticity

The treatment of ellipticity followed that of FWHM values; although a reliable measure of field-wide ellipticity was determined from the median of the best-fit FWHM values across the field and the relation

$$e = 1 - \frac{\text{FWHM}_{\text{min}}}{\text{FWHM}_{\text{maj}}} \quad (5)$$

(where FWHM_{min} and FWHM_{maj} are the full-width half-maxima along sources' semi-minor and semi-major axes respectively).

Fig. 9 shows the distributions of ellipticities as determined by Equation 5 and the FWHM values determined in Section 3.4.2. The median ellipticity value as determined by IMCORE is denoted by a red line. It can be seen that the median values for three of the four test fields are slightly optimis

tic (i.e. underestimate the ellipticities measured from 2D Gaussian fits). Owing to the fact fields displaying ellipticities greater than 0.3 were excluded from release in DR2, the slight mismatch between the median of the fitted ellipticities and the comparatively optimistic median calculated by IMCORE will never be so large that it will significantly affect the recovery of sources.

Seems a bit weak. But returned magnitude shouldn't really be affected by ellipticity - we're not PSF fitting each source. Position might be affected, but only by a very small amount.

3.4.4 Position angle

Conclusion in thesis is that most fields' PA distributions are too flat (or at least not nicely Gaussian) to confidently obtain a PA, so it's dropped. Is such a subsection even worth including here?

3.4.5 Position

Object x and y pixel positions were drawn randomly from uniform distributions across the 2048×4096 pixels of the WFC CCDs.

As the completeness calculated for CCD 4 of each field was taken as representative of the completeness over all four chips, the only problem region in placing sources was the border regions. *Include plot of used region of all 4 CCDs here or in map generation section.* A $10''$ border was excluded around the CCD edge; this area potentially contains truncated sources, and as such was not permitted to contribute sources to the density map.

3.5 Recovery of simulated sources

Cross-matching the recovered sources to the added artificial sources required the imposing of matching thresholds in both position and brightness. While a recovered source should lie centred on the exact x, y pixel position where it was added, there is no guarantee that IMCORE will report its centroid to lie at these coordinates. Background variations in the original image and pixel binning may cause the reported centroid to shift by a small amount; a generous threshold was adopted of 5 pixels from the recorded position of inserted sources.

Simply cross-referencing the recorded position of an artificial source with the new set of catalogues was not sufficient to ensure that a source had been successfully recovered. Including the magnitude of the source inserted in the comparison added an additional constraint which helped to reduce spurious crossmatches between the artificial source and pre-existing nearby sources of different magnitudes.

Choosing threshold an on offset in magnitude space (Δ_m) was more involved than in pixel position. Previous attempts to use artificial photometry in this way have faced similar issues; Mateo & Hodge (1986), as part of a study of a globular cluster in the LMC, added artificial stars to their images using DAOPHOT. They considered a source recovered if an source was returned at the same coordinates within 0.5 mag. Harvey et al. (2006) used this approach in a study of stellar sources in the Serpens molecular cloud,

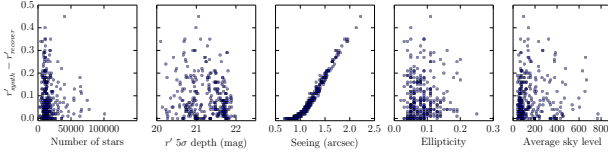


Figure 10. Modal difference between artificial inserted and recovered magnitude difference per field, plotted against field parameters.
textslRedo this plot with only seeing panel. Or could drop entirely.

and plotted the average difference ($|m_{\text{obs}} - m_{\text{injected}}|$) for artificial sources injected into their data, finding a range from 0.1 mag at ~ 10 -13 mag to more than 0.5 mag at ~ 15 mag.

For each field, the distribution of Δ_m values was binned and the modal value determined. For a number of fields, the modal value reached ≈ 0.4 mag - an effect that would require a Δ_m tolerance of > 0.5 mag. Such a large tolerance would likely result in many spurious cross-matches and hence an unduly optimistic estimate of completeness fractions, especially at fainter magnitudes.

In the course of investigating whether field conditions correlated with the offset of the Δ_m distribution, the modal shift value for each field was plotted against a number of field parameters. The resulting plots, seen in Fig. 10, clearly show that the remaining offset to the recovered magnitudes correlates with increasingly poor seeing conditions.

Poor seeing was found to affect the measured PSF such that the returned magnitudes from an image were offset by a uniform amount rather than having their spread increased - this is illustrated by the tightness of the correlation between Δ_m values and seeing, up to the highest seeing values encountered in the survey. This justified the application of a uniform shift to all measured magnitudes from an image, applied to bring the median Δ_m of a field to zero.

Having reduced the systematic shifts to Δ_m values, a threshold value needed to be chosen for considering an artificial source recovered. As illustrated in Fig. 11, the completeness curves remain relatively unchanged at $r' \lesssim 19$ as the Δ_m threshold is varied between 0.5 and 0.1 mag (the magnitude range of interest for correcting the density map). A threshold value of 0.25 mag was chosen as a compromise between avoiding admitting a large number of spurious detections at the faint end of the magnitude distribution, and ensuring that few objects are missed due to the occasional large Δ_m value.

3.6 Completeness fractions

Fig. 12 shows the completeness curves of all DR2 fields; the discrete quantisation of completeness is more prominent at the bright end due to lower artificial sources being injected to assess the incompleteness of bright sources. The upper two cumulative histograms shown in 12 show that incompleteness remains low at bright magnitudes, with a median completeness of 99.5% at $r' = 15$. At 18th magnitude the median completeness of IPHAS is 97.7% complete, falling to a median completeness of 93.1% at 20th magnitude.

In order to apply completeness corrections when generating the density map, each detected source needs to con-

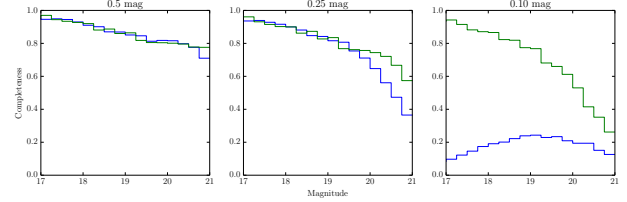


Figure 11. r' -band completeness fractions (green) for IPHAS field 4121o.jul2009, with offset tolerances between inserted and recovered magnitudes of 0.5, 0.25, and 0.1 mag (from left to right). **Blue:** Completeness fraction before implementing the scaling to total flux vs. magnitude relation (see Section 3.4.1) and the shift to account for the effect of seeing (see Section 3.5). **Green:** Completeness fraction after applying these corrections.
The point of this plot is currently to emphasise the effect of scaling to total flux rather than peak height. But if we're not mentioning peak height at all then this plot should be regenerated with only the green lines, to show the effect of changing matching tolerance.

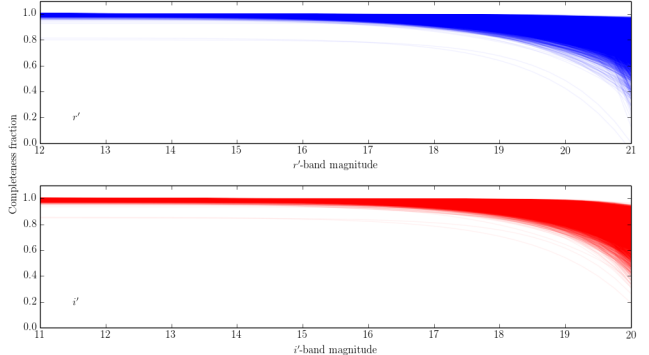


Figure 13. Best fits to completeness curves (as illustrated in Fig. 12) for both r' (upper) and i' (lower) catalogues.

tribute to the map by a factor that takes into account the incompleteness of sources of similar magnitude from its field of origin. In order to characterise the incompleteness fraction of each field as a quantity varying continuously with magnitude, a function was fit to the measured completeness fractions of each field, of the form

$$C(r') = \alpha - \gamma \times e^{\frac{r'}{\beta}} \quad (6)$$

where α , β , and γ are parameters allowed to vary to find the best fit for each field. These parameters were collected and formed a lookup table for use in correcting the density map. The curves of this form can be seen plotted for every field in Fig. 13.

As mentioned in Section 3.4, the completeness curves generated from CCD 4 of each field were used to represent those of the field as a whole. To ensure that this approach was sensible, a random set of fields had completeness curves generated for all four CCDs in order to compare completeness curves and ensure that the variation between chips was acceptably low. For the magnitude range $12 < r' < 21$, standard deviations in the completeness corrections were calculated. At $r' = 19$, the deviation in completeness corrections between CCDs reaches as high as 0.025 - these cases occur

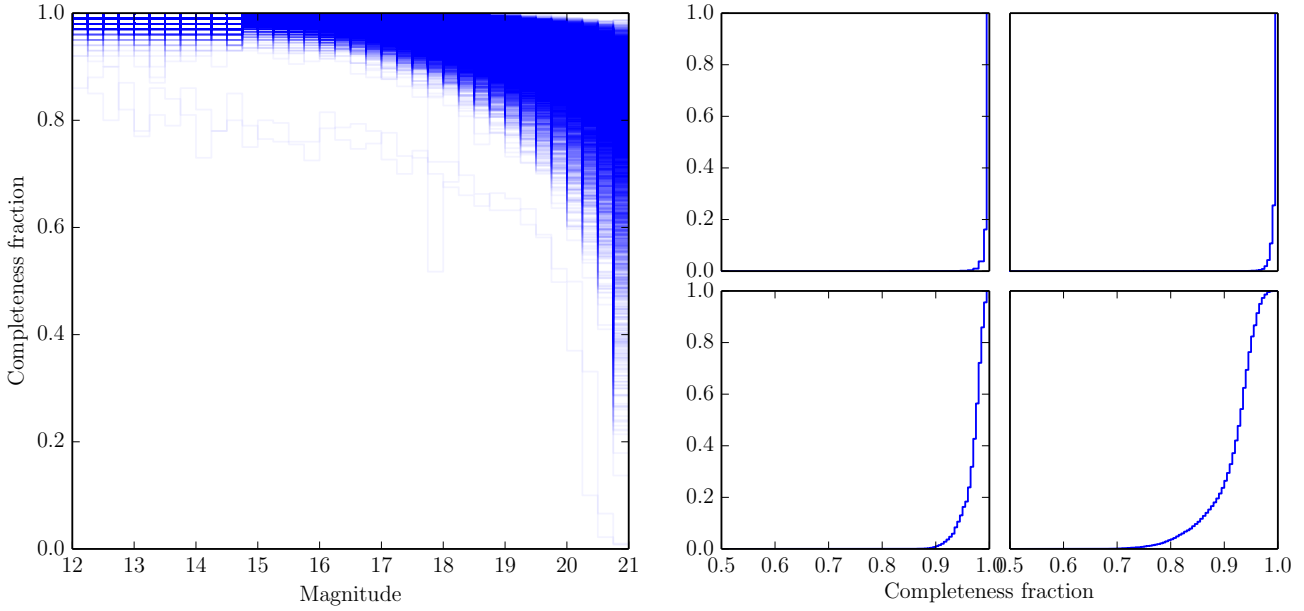


Figure 12. **Left:** Plot of every completeness curve in DR2, for magnitude bins of width 0.25 in range $12.0 < r' < 21.0$. **Right:** Cumulative histograms of field completeness for magnitude bins **a)** $12.0-12.25$, **b)** $15.0-15.25$, **c)** $18.0-18.25$, **d)** $20.0-20.25$. *Regenerate leaving out Capella-afflicted field pairs!*

where a bright star appears in one or more CCD of the field. These cases are rare; the median σ at $r' = 19$ is 0.005.

4 THE DENSITY MAPS

Cut down contents of Chapter 5, describing how sources are counted, resolutions/limits available.

4.1 Source counting

The IPHAS footprint was split into cells of the desired resolution (the final cell size was $1' \times 1'$), and for each cell, a table identifying the extent of every image contributing to DR2 (at the CCD level, i.e. $4 \times$ sub-images distinguished per field) was queried to identify which intersect the cell (either completely or in part). In order to calculate the coverage of each CCD, the pixel coordinates of each corner were determined, with an unusable border region taken into account for each of the four CCDs, in order to exclude sources detected far from the WFC optical axis (source counts from these regions would be unreliable). Fig. 14 shows the extents of the CCDs that were included when calculating coverage.

For each cell, the relevant files identified in by the coverage table was accessed, and all sources within the cell boundaries selected from the intersecting fields. Sources meeting the following criteria were retained:

- Morphology classification -1, -2 or +1
- Brighter than faint limit (default $r' = 19$)
- Flag errBits < 64 for band of interest

where the errBits criterion eliminates sources with bad pixels within their PSF, which are truncated, or which are vi-

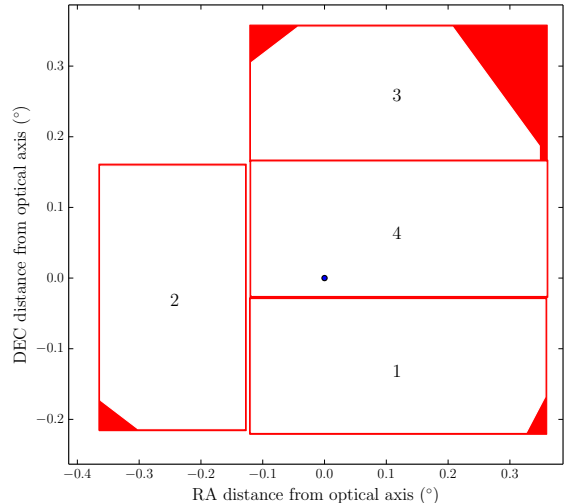


Figure 14. Area discarded when calculating coverage of density map cells by IPHAS CCDs contributing to DR2. Blue point denotes optical axis of the WFC. CCD chips are numbered.

gnected. The exclusion zone shown in Fig. 14 will have eliminated the majority of such cases, while this pass removed sources affected by issues such as bad columns and hot pixels.

For each remaining source, a *corrected contribution* to the number count of the cell was computed from the completeness curves generated in Section ???. The table containing α , β , and γ values (defining Eqn. 6) for each field was

read in, the values relevant to the current field identified, and the magnitude of the source under consideration used to calculate the corrected contribution. The original (ϕ) and corrected (Φ) source counts were recorded, along with the area of the intersection between the cell and the IPHAS field. Each estimate of total cell occupation, Φ' is given by

$$\Phi' = \frac{\Phi}{\text{coverage fraction}} \quad (7)$$

and the estimate of uncertainty is simply the Poisson noise of the observed area scaled to the cell:

$$\Phi'_{\text{err}} = \frac{\sqrt{\Phi}}{\text{coverage fraction}}. \quad (8)$$

This is repeated for each CCD covering the cell, and for each cell in the density map.

This method of populating density map cells provides additional information compared to the averaging of repeated sources. At $1' \times 1'$ resolution, the density map contains 6,537,051 cells overlapping with IPHAS photometry. Of these, 92.9% have an overlap with a second IPHAS CCD, with 38.3% having a third. These cells provide an estimate of the variance in source counts between observations, which in turn can be compared with the Poisson uncertainty calculated for these cells. *Ref section that contains this discussion.* In cases where multiple CCDs covered the same fraction of a cell, the count from the CCD observed under the best conditions was used to inform the density map.

4.2 Bright stars

The fact that the r' - and i' -band maps are generated independently means that spurious sources detected in one filter can be included in the map. The majority of such sources are noise and as such are eliminated based on their morphological classification. However in the regions surrounding bright stars ($V \lesssim 3$), the scattered light produced can lead to a large number of spurious detections which are classified as stellar or extended sources. Crossmatching between bands to eliminate such detections is not an option, as this would eliminate redder sources included in the i' -band map.

Around fainter stars ($V \lesssim 5$) the scattered light is not as severe as to increase the number of spurious sources; rather a zone of missing sources is observed due to the saturation caused by these stars. This incompleteness is more localised than taken into account by the approach of §3.

In order to avoid the issues discussed above, cells laying within $5'$ of stars brighter than $V = 5$ appearing in the catalogue of Hoffleit & Jaschek (1991) were excluded from the density map. As a result, 0.2% of the density map cells were discarded.

4.3 Uncertainty

Cells which are covered by IPHAS but contain no sources (i.e. are genuinely empty down to the adopted faint limit) have an uncertainty placed on them equal to the contribution of a single source at the faint limit of the density map.

For cells covered by multiple CCDs, the availability of repeated source counts allows the impact of per-field incompleteness corrections on the reliability of the density maps to be assessed. Comparing the scaled Poisson uncertainty

	17.0	17.5	18.0	18.5	19.0	19.5	20.0
r'	-	-	1	2	3	4	5
i'	1	2	3	4	5	-	-

Table 2. The FITS extension corresponding to faint limiting magnitudes for both r' - and i' -band density maps.

on the adopted cell count to the variance between counts from independently corrected CCD contributions revealed that the variance was smaller than the Poisson uncertainty in the vast majority of cases. This implies that the incompleteness correction did not introduce a significant source of uncertainty into the map; in fact the Poisson uncertainty provides a somewhat pessimistic view on the performance of the density map.

The median source count across all r' -band density map cells (the distribution shown in Fig. ??) is ≈ 6.2 , corresponding to $\approx 20,000$ sources per sq. deg.. Assuming that over $1' \times 1'$ cells that the source densities are uniformly distributed, on average 16% of the area of any one cell would need to be covered in order to detect a single source - if less than this area were covered, the source count would be unreliable. Taking the expected uncertainty for an empty cell (typically ≈ 1.2 at $r' = 19$) and rounding up the minimum acceptable cell coverage fraction to 20%, a limiting scaled error of 6 counts for an empty cell is obtained. Any unoccupied cells with greater error were discarded as being unreliable.

4.4 Final map availability

Cutouts of the final i' -band density map can be seen in Fig. 16. The three sightlines shown illustrate the variation in stellar densities across the Galactic Plane; the inner Galaxy sightline contains some of the lowest and highest density cells in the entire map, while the $80^\circ < \ell < 90^\circ$ and anticentre sightlines illustrate the declining densities towards the outer disc.

Both r' - and i' -band density maps are available at a variety of depths and resolutions. At each resolution the maps are stored as multi-extension FITS files, with extensions containing maps of increasingly faint limiting magnitude. Table 2 lists which extension corresponds to which faint limit for each band.

5 TESTING AGAINST MODELS

The Besançon model (Robin et al. 2003) is designed to generate synthetic Galactic populations, combining knowledge of the Milky Way from several sources. The model predictions are based on assumptions of a number of quantities, including density laws, star formation rates and initial mass function.

The Besançon model is one of the tools that will be used to interpret Gaia data, and is being updated to incorporate the latest developments in studies of Galactic evolution, structure and kinematics (Czekaj et al. 2014). However the 2003 model has been used extensively (*a few references*)

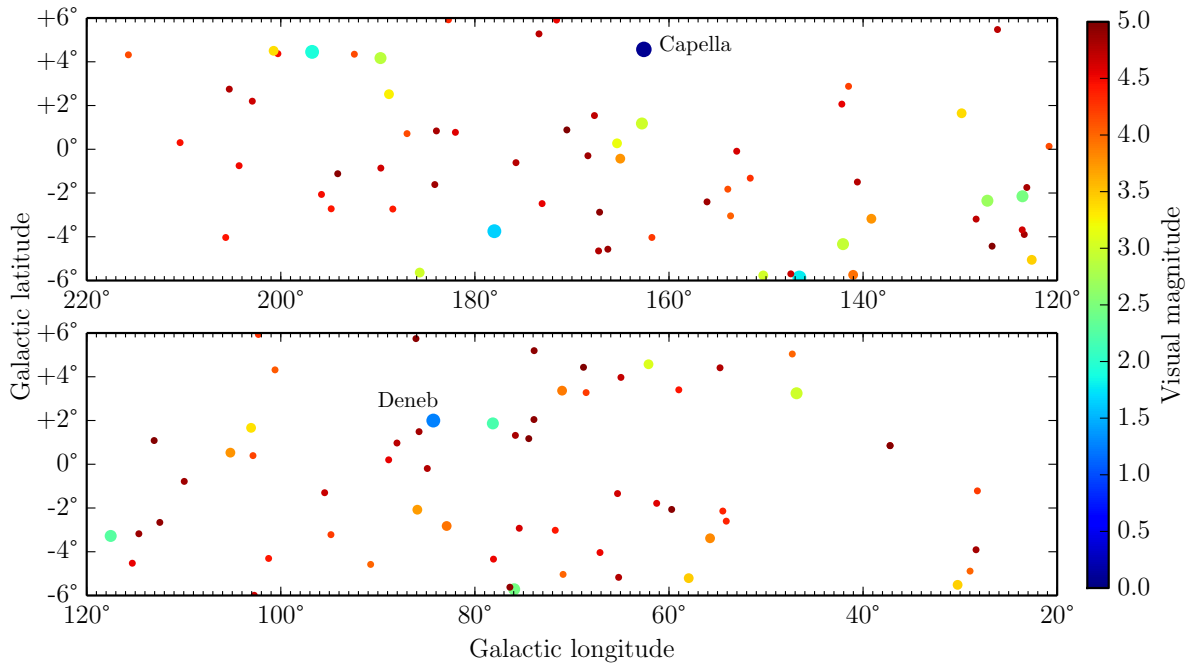


Figure 15. Distribution of bright ($V \leq 5$) stars in the Galactic Plane, based on the catalogue of Hoffleit & Jaschek (1991). Symbol size, as well as colour, is scaled to visual magnitude.

and offers downloadable synthetic catalogues - for this reason it was adopted for comparisons against IPHAS stellar densities.

5.1 Querying the Besançon model

The Besançon model as presented in Robin et al. (2003) is made available for use through a set of web pages¹, which can be used to generate synthetic catalogues based on a series of criteria. The region over which objects are simulated can be specified in both heliocentric distance and Galactic coordinates, extinction parameters can be modified, spectral types and absolute magnitude ranges can be selected, and limits based on apparent magnitudes imposed. Two output photometric systems are available: Johnson-Cousins and CFHTLS-Megacam. Fortunately the Megacam filters were designed to closely replicate the SDSS filter set, meaning catalogues output by the Besançon website can be sensibly compared with IPHAS. The IPHAS/SDSS transformations presented in Barentsen et al. (2014) were applied to bring the returned synthetic magnitudes into the IPHAS photometric system.

The web interface places limits on the region of sky that can be simulated in a single simulation, preventing the filesizes of resulting catalogues from becoming too large. In order to simulate a significant ($>$ a few sq. deg.) region of the Galactic Plane, a script was used to make repeated small ($\ll 1$ sq. deg.) requests, moving across the area

of interest, thereby building up a larger catalogue. The diffuse extinction parameter was set to zero, allowing custom distributions to be applied later (see Section 5.3). Querying small regions of the Galactic Plane produced results so quickly (in a minute, roughly) that all populations of sources were included, and the default absolute magnitude range ($-7 < M < 20$) retained. An apparent magnitude range of $8 < r' < 25$ was imposed to exclude any objects falling far outside IPHAS detection limits. Options for including kinematics are also available but were not used here.

While the Besançon model adopts a thin disc with a hole at its centre, its effect can be neglected as even at the lowest Galactic longitudes covered by IPHAS, the sightlines towards the inner Galaxy have their closest approach (*4 kpc - check!*) to the Galactic Centre outside the affected region (their adopted hole scalelength is 1.3 kpc.).

5.2 Sightlines

Regions of 20 sq. deg. were chosen for the comparison based on the coverage of the density maps; areas at $\ell \approx 30^\circ$, 90° , and 175° were simulated via the Besançon web interface, and the stellar densities of the corresponding regions in the IPHAS i' -band density maps were extracted.

Fig. 17 shows the variation in stellar densities with Galactic latitude in these regions, as retrieved from the $20' \times 20'$ resolution IPHAS i' -band density map. Each sightline was split into two 1° -wide strips in Galactic longitude to prevent the blurring of structure in the disc; variation on these scales can be seen by comparing the densities in the

¹ <http://model.obs-besancon.fr/>

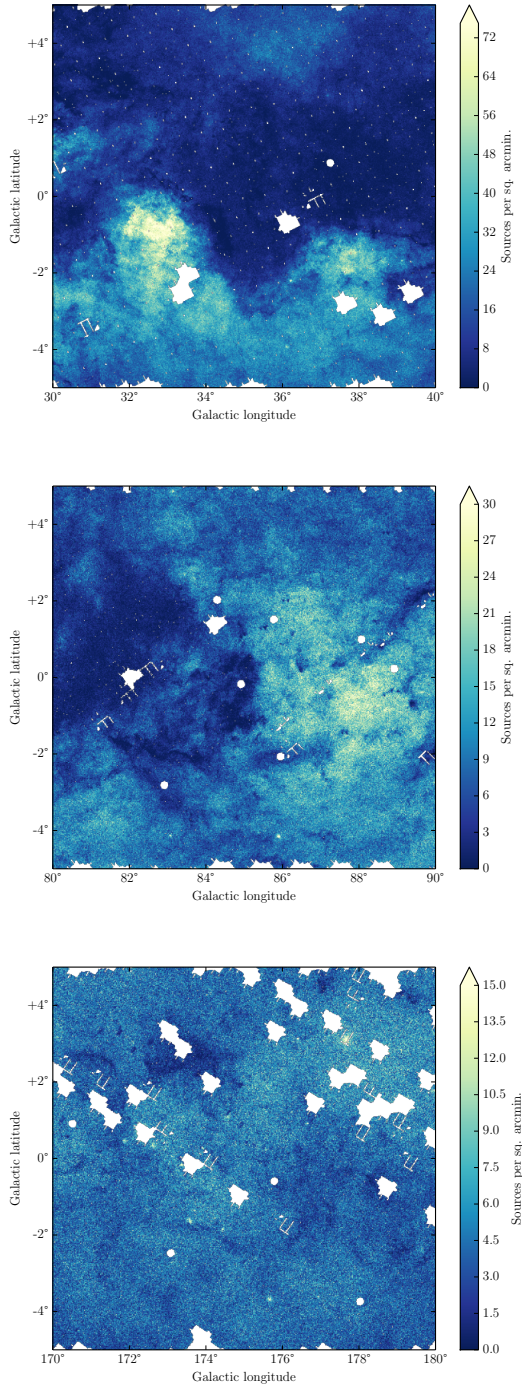


Figure 16. Cutouts of the i' -band density map with $1' \times 1'$ resolution. Upper: Inner Galaxy sightline showing the Aquila Rift. Middle: Sightline covering the Cygnus region. Lower: Anticentre sightline.

two strips. Fig. 18 shows the sightlines and how they relate to spiral arms according to the model of Vallée (2008).

The inner Galaxy sightline shows the largest variation with latitude and the largest variation between the two separated 1° -wide strips. The Aquila region ($\ell \lesssim 45^\circ$) contains both the highest and lowest valued cells of the entire IPHAS

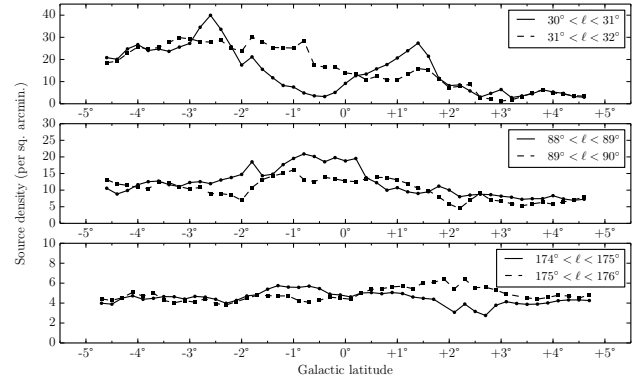


Figure 17. Stellar density profiles in Galactic latitude, averaged over 1° wide strips in Galactic longitude, as given by the $20' \times 20'$ resolution IPHAS i' -band density map. Each panel shows two profiles for each sightline to be compared against star counts predicted by the Besançon model.

density map. A dark cloud at ($\approx 30^\circ, -1^\circ$) is responsible for the reduction in stellar density (of the amplitude $\approx 10 - 20$ sources per sq. arcmin.) in the $30^\circ < \ell < 31^\circ$ profile relative to the $31^\circ < \ell < 32^\circ$ profile. The Aquila Rift is responsible for the drop-off in stellar density at higher latitudes in both strips. Taking the spiral arm positions of Vallée (2008), it can be seen (in Fig. 18) that this sightline will pass through the Sagittarius-Carina arm twice by a distance of 10 kpc, and passes through the tangent of the Scutum-Crux arm; such spiral arm crossings are likely to render the extinction distribution in this direction quite complex.

The sightline towards $\ell = 90^\circ$, bordering the Cygnus region ($60^\circ \lesssim \ell \lesssim 90^\circ$), shows more pronounced variation with latitude, and greater variation between the two strips. Further from the Galactic midplane the two seem to be in good agreement. The spiral arm predictions of Vallée (2008) place the Perseus arm at ≈ 4 kpc in this direction.

The anticentre sightline shows the least variation- at positive latitudes showing a difference of ≈ 2 per sq. arcmin. between the two strips. The flatness of the distributions highlight the relative lack of structure apparent in the density map at these longitudes; this suggests that the Besançon model is likely to perform well along this sightline - an exponentially decreasing stellar density with galactocentric radius has the potential to capture the observed smooth behaviour. A potential deviation from a smooth distribution comes from the Perseus Arm, predicted by Vallée (2008) to lie at a distance of ≈ 2 kpc at this longitude.

5.3 Adding extinction

With the diffuse extinction parameter set to 0 mag kpc^{-1} , the synthetic catalogues returned provided an unreddened view of the Milky Way. As the catalogues provide the distance to each generated object, a custom extinction profile could be imposed on the catalogued sources. Four different extinction prescriptions were applied to the catalogues, as detailed below.

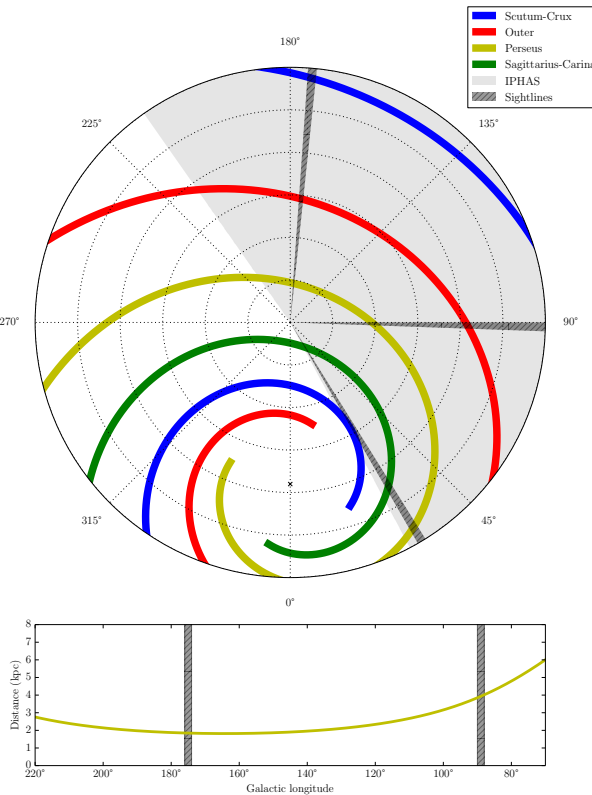


Figure 18. Upper: Distribution of spiral arms in Galactic coordinates, with distance from the Sun to the spiral arms based on the parameters obtained by Vallée (2008). Dotted circles denote distances in increments of 2 kpc. The Galactic Centre is shown as a black cross. The region covered by IPHAS is highlighted in gray. The sightlines compared with Besançon model predictions are denoted by darker hatched regions. **Lower:** Distance to the Perseus arm in the range $70^\circ < \ell < 220^\circ$ based on the parameters of Vallée (2008); this spiral arm is expected to be the main discrete feature likely to influence the observed star counts at $\ell \gtrsim 60^\circ$. The two IPHAS sightlines compared to Besançon model predictions in this region are marked by gray hatched regions.

5.3.1 Marshall extinction map

The extinction map produced by Marshall et al. (2006) were applied to the catalogues, taking the sightline closest to the synthetic catalogue coordinates - the Marshall et al. (2006) sightlines are binned in 0.25° increments in Galactic longitude and latitude. They provide curves only for sightlines with $\ell < 100^\circ$; comparisons in the outer disc do not involve this model. The extinction in this model is given for the K_s band (A_{K_s}) as a function of distance, values which were converted to $A_{i'}$ using the extinction law of Cardelli et al. (1989) (using the conversion factors for K and I filters, giving $A_{i'} = 4.2A_{K_s}$).

5.3.2 Sale extinction map

The 3D map of Sale et al. (2014) are the result of combining IPHAS DR2 photometry with the hierarchical Bayesian model developed in Sale (2012), which estimates the distance-extinction relationship along a given sightline, along with estimates of stellar parameters of the stars sam-

pled. The priors adopted by this approach assume all sightlines consist entirely of thin disc stars, with a scalelength of 3 kpc.

The map provides a typical angular resolution of $10'$; the nearest sightline to the Besançon catalogue under consideration was used to extinguish the synthetic photometry. While each sightline is provided with a maximum reliable distance, assuming the final value beyond these limits would result in underestimations of extinction at larger distances. For this reason, entire sightlines were used. Being based on IPHAS photometry, all the sightlines considered fall into the area covered by the map.

5.3.3 Perseus model

The extinction values provided by Schlegel et al. (1998) are integrated values along the line of sight - no radial information is provided that would allow the extinguishing material to be placed along a given sightline. As a simple model of the ISM for sightlines passing through the Perseus arm, the majority of the extinction was attributed to its position, after assigning an amount of local extinction ($d < 600$ pc) based on the measurements of Lallement et al. (2014). The location of the Perseus arm was determined from the parameters of the spiral arms obtained by Vallée (2008), as shown in Fig. 18. Taking a spiral arm half-width of 400 pc (Vallée 2014) and modelling the dust distribution across the arm as a Gaussian, the total extinction of Schlegel et al. (1998) (recalibrated by Schlafly & Finkbeiner (2011)), less the extinction accounted for locally, was assigned across this pseudo-Perseus arm.

As illustrated by Fig. 18 sightlines in the IPHAS footprint become more complicated at $\ell \lesssim 60^\circ$, as they pass through multiple spiral arms. For this reason the Perseus model was limited to sightlines passing through the Perseus (and potentially Outer) Arm only.

5.3.4 Exponential disc model

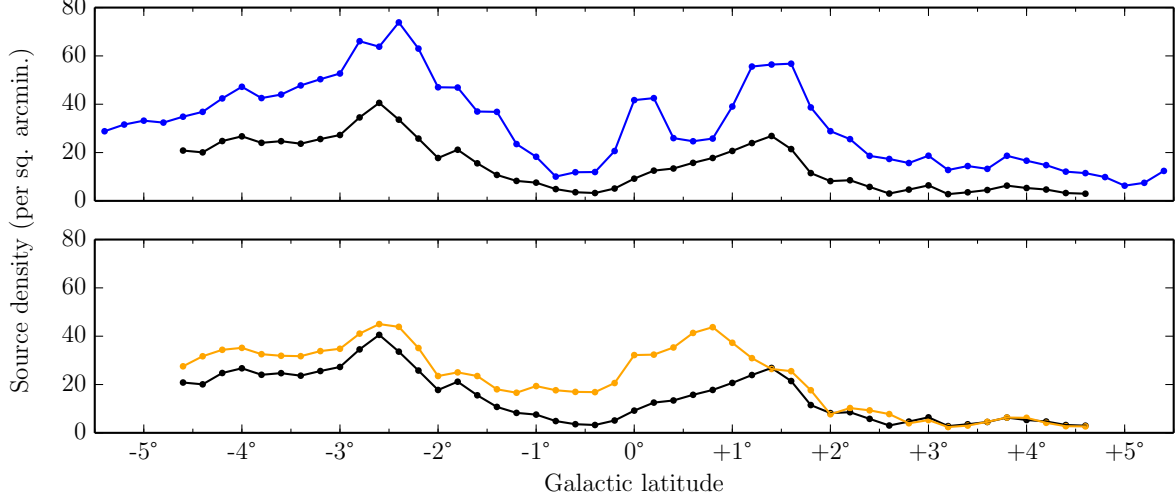
The default extinction model when using the Besançon web interface is an exponential disc of obscuring material, with a local extinction normalisation of 0.7 mag kpc^{-1} - it is noted that this value should be treated with caution in the Galactic Plane. In order to reproduce a similar extinction model, a disc of obscuring material was imposed on the Besançon catalogue. The local A_0 (monochromatic extinction at 5495\AA) normalisation was determined by imposing discs with normalisations ranging from 0 to 3 mag kpc^{-1} in steps of 0.05 mag kpc^{-1} , to the Besançon catalogue along each sightline. The magnitude distribution of bright ($12 < r' < 15.5$) stars in the resulting extinguished synthetic catalogue was compared to the corresponding IPHAS DR2 distribution in the same area. The local normalisation that resulted in the best agreement between the two magnitude distributions was adopted for the sightline.

5.4 Comparing IPHAS and Besançon densities

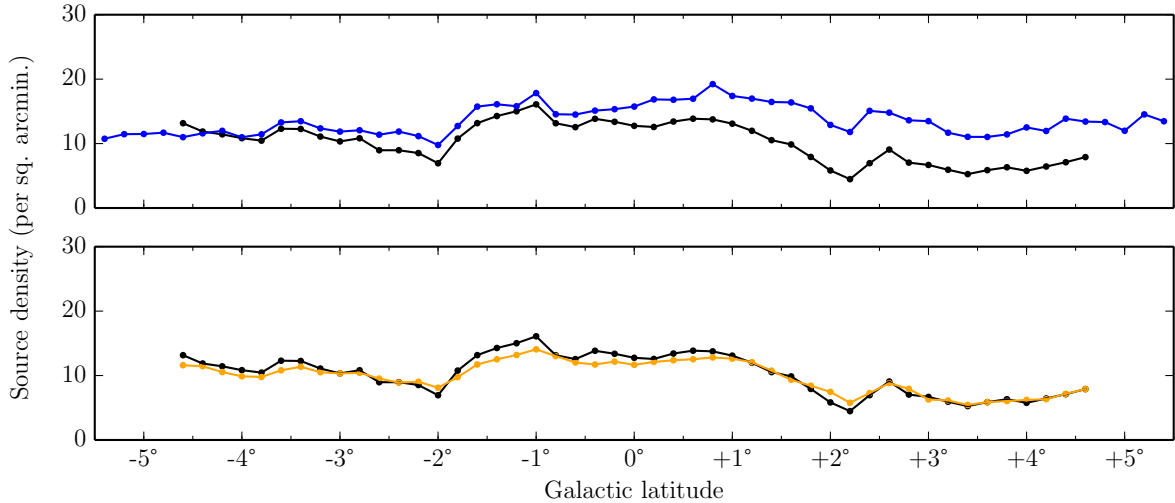
REFERENCES

- Bahcall J. N., 1986, *ARA&A*, 24, 577
 Barentsen G. et al., 2014, *MNRAS*, 444, 3230

$\ell=30^\circ$:



$\ell=90^\circ$:



$\ell=175^\circ$:

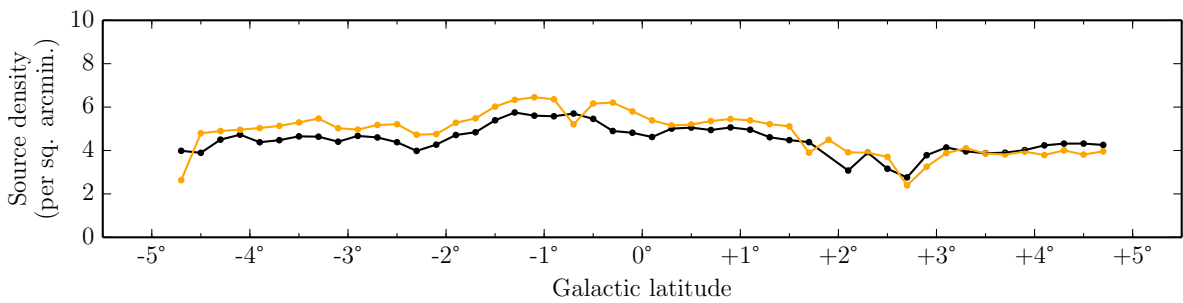


Figure 19. Comparisons between incompleteness-corrected IPHAS star counts (black) and Besançon predictions, reddened by the extinction curves of ? (blue) and Sale et al. (2014) (yellow). From top to bottom, comparisons are for sight lines at $\ell=30^\circ$, 90° and 175° .

Cambrésy L., Beichman C. A., Jarrett T. H., Cutri R. M., 2002, AJ, 123, 2559
 Cardelli J. A., Clayton G. C., Mathis J. S., 1989, ApJ, 345, 245
 Condon J. J., 1974, ApJ, 188, 279
 Czekaj M. A., Robin A. C., Figueras F., Luri X., Haywood

M., 2014, A&A, 564, A102
 González-Solares E. A. et al., 2008, MNRAS, 388, 89
 Harvey P. M. et al., 2006, ApJ, 644, 307
 Hoffleit D., Jaschek C. V., 1991, The Bright Star Catalogue, 5th edn., Hoffleit D., Jaschek C., eds. Yale Univ. Obs., New Haven, Conn.

- Irwin M. J., Trimble V., 1984, AJ, 89, 83
 Lallement R., Vergely J.-L., Valette B., Puspitarini L., Eyer L., Casagrande L., 2014, A&A, 561, A91
 Lucas P. W. et al., 2008, MNRAS, 391, 136
 Marshall D. J., Robin A. C., Reylé C., Schultheis M., Picaud S., 2006, A&A, 453, 635
 Mateo M., Hodge P., 1986, ApJS, 60, 893
 Robin A. C., Reylé C., Derriere S., Picaud S., 2003, A&A, 409, 523
 Ruphy S. et al., 1997, A&A, 326, 597
 Sale S. E., 2012, Monthly Notices of the Royal Astronomical Society, 427, 2119
 Sale S. E. et al., 2014, MNRAS, 443, 2907
 Schlafly E. F., Finkbeiner D. P., 2011, ApJ, 737, 103
 Schlegel D. J., Finkbeiner D., Davis M., 1998, ApJ, 500, 525
 Vallée J. P., 2008, AJ, 135, 1301
 Vallée J. P., 2014, AJ, 148, 5
 Yasuda N. et al., 2001, AJ, 122, 1104

APPENDIX A: ARTIFICIAL OBJECT INSERTION FOR TESTING COMPLETENESS

Algorithm / figure showing processing steps

APPENDIX B: IPHAS/GAIA TRANSFORMATIONS

Could be useful?